

On Low-Dimensional Modeling of Channel Turbulence¹

Ahmet Omurtag and Larry Sirovich

Laboratory of Applied Mathematics, Box 1012, CUNY/Mt. Sinai,
New York, NY 10029, U.S.A.
{ahmet,chico}@camelot.mssm.edu

Communicated by M.Y. Hussaini

Received 13 July 1998 and accepted 8 January 1999

Abstract. We investigate a sequence of low-dimensional models of turbulent channel flows. These models are based on the extraction of the Karhunen–Loève (KL) eigenfunctions from a large-scale simulation in a wide channel with $R_* = 180$ (based on the friction velocity). KL eigenfunctions provide an optimal coordinate system in which to represent the dynamics of the turbulent flow. The hierarchy of KL modes identifies the most energetic independent phenomena in the system. A series of Galerkin projections is then used to derive a dynamical approximation to flows. In order to capture essential aspects of the flow in a low-dimensional system, a careful selection of modes is carried out. The resulting models satisfy momentum and energy conservation as well as yielding the amount of viscous dissipation found in the exact system. Their dynamics includes modes which characterize the flux, rolls, and propagating waves. Unlike previous treatments the instantaneous streamwise flow is time dependent and represented by KL flux modes. The rolls correspond to the streaks observed in experiments in the viscous sublayer. Propagating waves which first appear in the model flow at low Reynolds number ($R_* \sim 60$) persist through the chaotic regime that appears as the Reynolds number is increased. Statistical measures of the chaotic flows which have been generated by the models compare favorably with those found in full-scale simulations.

1. Introduction

We consider a fluid forced to move along an infinite channel by a steady pressure gradient or, equivalently, a body force. At sufficiently high Reynolds numbers, turbulence sets into the flow. The energy introduced into the fluid results in a time-dependent net flux as well as in irregularly fluctuating velocity components. In such wall-bounded turbulent flows, mean quantities take on standard spatial distributions. In addition, coherent structures, relatively large energy-bearing modes, are known to exist. Some of this energy can be associated with a cascade process similar to that in homogeneous isotropic turbulence [1], [2]. A diverse collection of studies (e.g., [3]–[5]) suggest that such turbulent flows lie on a strange attractor of (relatively) small dimension. This suggests that a low-dimensional description may be plausible. This is the direction taken in a number of studies [6], [7].

In this paper we investigate a set of low-dimensional descriptions constructed by approximating the fluid's velocity field $\mathbf{u}(\mathbf{x}, t)$ along with its evolution equation (in this case the incompressible Navier–Stokes equations) by means of a set of orthonormal functions $\{\mathbf{V}^m(\mathbf{x})\}$. For a proper description, the choice of functions \mathbf{V}^m constitutes an important step. By well-defined criteria explained further below, Karhunen–Loève (KL) or empirical eigenfunctions [8] (or [9] and [10]) are best suited for this task. We note, in

¹ This work was supported in part by Grant AFOSR F49620-98-1-0294 with Brown University.

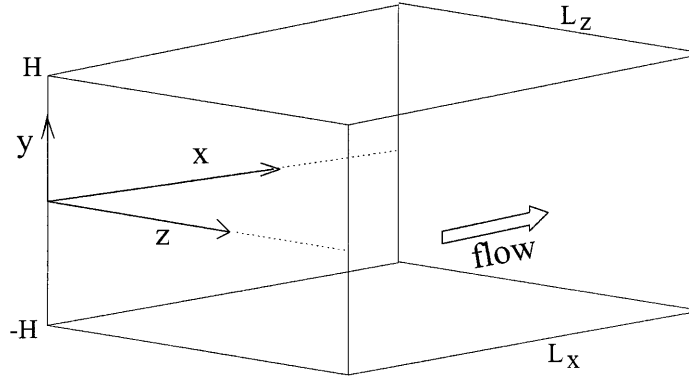


Figure 1. The Cartesian coordinate system of the computational volume.

particular, the properties of optimal convergence and the statistical independence of their coefficients. This approach was first adopted in a study of the Ginzburg–Landau equation [6], a model partial differential equation in fluid mechanics. In a number of other investigations, empirical eigenfunctions have been used in identifying coherent structures in turbulent flows as well as in modeling their dynamics [11], [7], [12]–[20].

In the present context, the homogeneity of the streamwise, x , and spanwise, z , directions reduces empirical eigenfunctions to Fourier modes. In order to resolve the cross-channel, y , variations in $\mathbf{u}(\mathbf{x}, t)$ we have utilized the results of a direct numerical simulation with $R_* = 180$ (based on wall scale) kindly provided by R. Moser. This computation was conducted with (x, y, z) -directions discretized as (128, 129, 128) with Fourier modes in the homogeneous directions and Tchebycheff polynomials in the y -direction. The domain is $L_x = 4\pi H$, $L_y = 2H$, and $L_z = 4\pi H/3$ (2300, 360, and 767, respectively, in wall units). The symmetries of the channel have been employed in increasing the size of the dataset used in calculating the KL eigenfunctions [21]. Through a careful selection of KL eigenfunctions we build and study a series of dynamical systems describing turbulent flow in the channel.

2. Formulation

2.1. Notation

We write $\mathbf{u} = (u, v, w)$ and $\mathbf{x} = (x, y, z)$ and consider the flow in the channel: $-\infty < x, z < \infty$; $-H < y < H$ driven by the gravity force k (or uniform pressure gradient) in the x -direction. The Navier–Stokes (NS) equations and boundary conditions are

$$\left. \begin{aligned} \nabla \cdot \mathbf{u} &= 0, \\ \rho \left(\frac{\partial}{\partial t} + \mathbf{u} \cdot \nabla \right) \mathbf{u} + \nabla p &= k \mathbf{e}_x + \mu \nabla^2 \mathbf{u}, \\ \mathbf{u}(x, y = \pm H, z, t) &= 0. \end{aligned} \right\} \quad (1)$$

Figure 1 shows a sketch of the coordinate system. In all our deliberations, the flow is taken to be L_x and L_z periodic in the x - and z -directions.

2.2. Normalizations

To normalize the problem we observe that a simple force balance shows that the wall skin friction τ satisfies

$$\tau = kH, \quad (2)$$

and therefore the friction velocity is given by

$$u_* = \sqrt{\frac{\tau}{\rho}} = \sqrt{\frac{kH}{\rho}}. \quad (3)$$

We normalize as follows:

$$\frac{\mathbf{u}}{u_*} \rightarrow \tilde{\mathbf{u}}; \quad \frac{\mathbf{x}}{H} \rightarrow \mathbf{x}; \quad \frac{tu_*}{H} \rightarrow t; \quad \frac{p}{\rho u_*^2} \rightarrow p; \quad (4)$$

in which case (1) becomes

$$\left. \begin{aligned} \nabla \cdot \tilde{\mathbf{u}} &= 0 \\ \frac{\partial \tilde{\mathbf{u}}}{\partial t} + \tilde{\mathbf{u}} \cdot \nabla \tilde{\mathbf{u}} + \nabla p &= \mathbf{e}_x + \frac{1}{R_*} \nabla^2 \tilde{\mathbf{u}} \\ \tilde{\mathbf{u}}(x, y = \pm 1, z, t) &= 0 \end{aligned} \right\} \quad (5)$$

with Reynolds number

$$R_* = \frac{u_* H}{\nu} = \frac{H}{l_*}, \quad (6)$$

where l_* is the wall scale. In (5) and thereafter $\tilde{\mathbf{u}}$, \mathbf{x} , t , and p refer to dimensionless quantities normalized as in (4).

2.3. Mean Flow

One definition of mean flow is

$$\mathbf{U}(y, t) = U(y, t)\mathbf{e}_x = \langle \tilde{\mathbf{u}} \rangle = \frac{1}{A} \int_A \tilde{\mathbf{u}}(\mathbf{x}, t) \, dx \, dz, \quad (7)$$

where $A = L_x L_z$. If $A \uparrow \infty$, then $\mathbf{U} = U(y)\mathbf{e}_x$, i.e., the mean flow becomes time independent. As pointed out in [5] and [19] finite area A forces a time dependence on the ‘‘mean flow’’ and in a number of formulations ignoring this fact lead to inconsistencies. It is our intention to treat this point with some care.

If we write

$$\tilde{\mathbf{u}}(\mathbf{x}, t) = \mathbf{U}(y, t) + \mathbf{u}(\mathbf{x}, t), \quad (8)$$

where \mathbf{u} now represents the departure from the flux \mathbf{U} and satisfies

$$\langle \mathbf{u} \rangle = 0, \quad (9)$$

it then follows that

$$LU = \left(\frac{\partial U}{\partial t} - \frac{1}{R_*} \frac{\partial^2 U}{\partial y^2} \right) = 1 - \frac{\partial}{\partial y} \langle uv \rangle. \quad (10)$$

The quantity $-\langle uv \rangle$ is the Reynolds stress, averaged over the portion of the x - z plane denoted A , and is therefore *time dependent*.

If (10) is substituted into (5) we obtain

$$\frac{\partial \mathbf{u}}{\partial t} + U \frac{\partial \mathbf{u}}{\partial x} + v \frac{\partial \mathbf{U}}{\partial y} + \mathbf{u} \cdot \nabla \mathbf{u} - \frac{\partial \langle uv \rangle}{\partial y} \mathbf{e}_x + \nabla p = \frac{1}{R_*} \nabla^2 \mathbf{u}. \quad (11)$$

If (10) is averaged in time, denoted by overbar we obtain

$$\frac{\partial}{\partial y} \langle \overline{uv} \rangle = 1 + \frac{1}{R_*} \frac{\partial^2 \overline{U}}{\partial y^2}, \quad (12)$$

which formally integrates to

$$\overline{U}(y) = R_* \int_{-1}^y \langle \overline{uv} \rangle \, dy + \frac{R_*}{2} (1 - y^2). \quad (13)$$

In the same formal sense the flux equation (10) is as indicated a linear operator and its solution may be written as

$$U(y, t) = L^{-1} \frac{\partial}{\partial y} \langle uv \rangle + \frac{R_*}{2} (1 - y^2). \quad (14)$$

The details of L^{-1} are straightforward. The set of functions $\{\sin(n\pi y)\}$ (integer n) is complete in the interval $-1 \leq y \leq 1$ and satisfies the boundary conditions. These may be used by standard methods to solve formally the inhomogeneous diffusion equation and hence to give L^{-1} explicitly.

The NS equations are equivalent to the coupled set of equations (10) and (11) for the mean flow and fluctuations, respectively. (10) may be solved to yield (14) which, substituted into (11), eliminates the mean flow. This gives a complicated cubic integrodifferential equation for \mathbf{u} . An alternative procedure [7], [9] for eliminating $U(y, t)$ involves assuming $\partial U / \partial t \approx 0$ in order to obtain an approximate and simpler solution of (10):

$$U(y, t) \approx R_* \int_{-1}^y \langle uv \rangle dy + \frac{R_*}{2} (1 - y^2). \quad (15)$$

This expression, which is the instantaneous counterpart of (13), implies that U is time dependent through $\langle uv \rangle$. As stated in [22] this is inconsistent with the assumption from which it is derived. Numerical results in model systems give strong time dependence of U in this formulation. In our model ODEs, the mean flow is *not* eliminated whether by the exact method using (14) or the approximate procedure. This is further elaborated in the final section.

2.4. Energy

If (10) is multiplied by U it can be put in the form

$$\frac{\partial U^2/2}{\partial t} = \frac{1}{R_*} \frac{\partial^2 U^2/2}{\partial y^2} - \frac{1}{R_*} \left(\frac{\partial U}{\partial y} \right)^2 + U - \frac{\partial(\langle uv \rangle U)}{\partial y} + \langle uv \rangle \frac{\partial U}{\partial y}, \quad (16)$$

which if integrated across the channel yields

$$\frac{\partial}{\partial t} \int_{-1}^1 \frac{U^2}{2} dy = -\frac{1}{R_*} \int_{-1}^1 \left(\frac{\partial U}{\partial y} \right)^2 dy + \int_{-1}^1 \langle uv \rangle \frac{\partial U}{\partial y} dy + 2U_b, \quad (17)$$

where we have defined the instantaneous bulk velocity as

$$U_b(t) = \frac{1}{2} \int_{-1}^1 U(y, t) dy. \quad (18)$$

The second term on the right hand side of (17) represents the total rate of kinetic energy absorbed by the fluctuating velocity field from the mean flow, the turbulence production.

3. Symmetries

The NS equations respect certain symmetries of the data. In particular, if the initial data is L_x -periodic in the x -direction and L_z -periodic in the z -direction, i.e.,

$$\tilde{\mathbf{u}}(x + L_x, y, z + L_z, 0) = \tilde{\mathbf{u}}(\mathbf{x}, 0) \quad (19)$$

then in the absence of perturbations the resulting solution inherits the same periodicity

$$\tilde{\mathbf{u}}(x + L_x, y, z + L_z, t) = \tilde{\mathbf{u}}(\mathbf{x}, t). \quad (20)$$

This property lies at the heart of numerical simulations. For the most part, in such simulations, the flow is taken to be periodic in the x - z plane. Thus the computation takes place in a computational volume, which in dimensional terms is given by $2HL_xL_z = V$.

There are other symmetries that involve the parity of the elements of $\tilde{\mathbf{u}}$. This can be discussed concisely in terms of the four-group of transformations under which the problem is invariant. Thus if $\tilde{\mathbf{u}}$ is a solution to (5), then

$$\left\{ \begin{array}{l} \tilde{u}(x, -y, z, t) \\ -\tilde{v}(x, -y, z, t) \\ \tilde{w}(x, -y, z, t) \end{array} \right\}, \left\{ \begin{array}{l} \tilde{u}(x, y, -z, t) \\ \tilde{v}(x, y, -z, t) \\ -\tilde{w}(x, y, -z, t) \end{array} \right\}, \left\{ \begin{array}{l} \tilde{u}(x, -y, -z, t) \\ -\tilde{v}(x, -y, -z, t) \\ -\tilde{w}(x, -y, -z, t) \end{array} \right\} \quad (21)$$

also satisfy (5) and each generates a new solution. The three flows of (21) along with $\tilde{\mathbf{u}}$ itself make up the flows generated by the four-group of symmetries.

The dynamical models which we will construct use databases generated from numerical simulations. If in the present notation $\tilde{\mathbf{u}}(\mathbf{x}, t) = \mathbf{U}(y, t) + \mathbf{u}(\mathbf{x}, t)$ represents such a solution, then the correlation

$$K_{ij}(\mathbf{x}, \mathbf{y}) = (\tilde{u}_i(\mathbf{x}, t), \tilde{u}_j(\mathbf{y}, t))_t \quad (22)$$

may be used to generate the empirical eigenfunctions [8] $\{\mathbf{V}^{(k)}\}$ from the eigenfunction analysis

$$\int K_{ij}(\mathbf{x}, \mathbf{y}) V_j^{(k)}(\mathbf{y}) d\mathbf{y} = \lambda_k V_i^{(k)}(\mathbf{x}). \quad (23)$$

These functions are orthonormal,

$$(\mathbf{V}^{(k)}, \mathbf{V}^{(l)})_{\mathbf{x}} = \int_V V_j^{*(k)}(\mathbf{x}) V_j^{(l)}(\mathbf{x}) d\mathbf{x} = \delta_{kl}. \quad (24)$$

In view of the translational invariance of the problem in the x - and z -directions these functions are sinusoidal in these directions. Specifically if the underlying simulation is L_x and L_z periodic in the x and z directions respectively then

$$\mathbf{V}^{(k)}(\mathbf{x}) \rightarrow \mathbf{V}^{\mathbf{m}}(\mathbf{x}) = \psi^{(m,n,q)}(y) e^{2\pi i(mx/L_x + nz/L_z)}. \quad (25)$$

Thus the indices m and n generate the wave numbers, $k_x = 2\pi m/L_x$ and $k_z = 2\pi n/L_z$, while q will be referred to as the vertical quantum number. Since $K_{ij}(\mathbf{x}, \mathbf{y})$ in (22) is real, both the real and imaginary parts of $\mathbf{V}^{\mathbf{m}}(\mathbf{x})$ are eigenfunctions of (23), corresponding to some (real) eigenvalue.

In such terms we can represent or analyze the flow through the decomposition

$$\tilde{\mathbf{u}}(\mathbf{x}, t) = \sum_{\mathbf{m}} a_{\mathbf{m}}(t) \psi^{\mathbf{m}}(y) e^{2\pi i(mx/L_x + nz/L_z)}. \quad (26)$$

A number of simulations have appeared in the literature, naturally at various R_* , but also for differing (L_x, L_z) . The latter has caused some confusion in the past and some attention to this point will be worthwhile. For example, in comparing the minimal channel simulation of Jimenez and Moin (JM) [23] with the channel calculation of Kim, Moin, and Moser (KMM) [24], then, roughly, the terms $L_z(\text{JM}) = \frac{1}{6}L_z(\text{KMM})$ and $L_x(\text{JM}) = \frac{1}{3}L_x(\text{KMM})$.

Suppose more generally that it is of interest to consider two flows \mathbf{u} and \mathbf{u}' for the same R_* such that

$$L'_x = \frac{1}{k}L_x, \quad L'_z = \frac{1}{l}L_z, \quad (27)$$

with k and l integers. If $\{\psi^{\mathbf{m}}(\mathbf{x})\}$ represents the KL basis for the unprimed flow then we can express the primed flow by

$$\tilde{\mathbf{u}}(\mathbf{x}, t) = \sum a_{\mathbf{m}}(t) \psi^{(km, ln, q)}(y) e^{2\pi i(kmx/L_x + lnz/L_z)}. \quad (28)$$

This decomposition is important in understanding the relationship between the two flows. The narrower shorter channel only requires a sparse set of the basis set (25). The indices m and n specify the number of cycles (*periods*) in the x - and z -direction. Thus, for example, in comparing JM with KMM, according to (27) the former requires three cycles in the x -direction and six cycles in the z -direction—and all integer multiples of these.

Another consequence of this discussion is that indices (m, n) should not be compared in flows of differing (L_x, L_z) . The appropriate kinematical comparison is in terms of wave numbers. Thus if

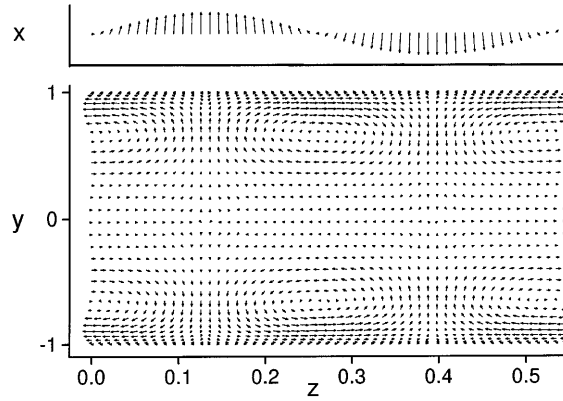


Figure 2. Part of the velocity field generated by the KL function $(m, n, q) = (0, 8, 1)$.

$(k_x, k_z) = (2\pi m/L_x, 2\pi n/L_z)$ and $(k'_x, k'_z) = (2\pi m'/L'_x, 2\pi n'/L'_z)$ are wave numbers for two channel flows, the *propagation directions* and *wavelengths* are the same if

$$\frac{m}{L_x} = \frac{m'}{L'_x} \quad \text{and} \quad \frac{n}{L_z} = \frac{n'}{L'_z}. \quad (29)$$

Appreciation of these simple minded observations can avoid some of the confusion that has appeared in the literature.

4. Flux, Roll, and Propagating Modes

As already mentioned only modes for which $m = n = 0$ contribute to the net flux of fluid in the streamwise directions. These modes are collected together in $U(y, t)$. If m or n is not zero there is no net flux of momentum in the streamwise direction. Since flux modes encompass the mean flow they naturally contain the overwhelming portion of the flow energy.

As for the remaining modes, those which show no streamwise dependence $m = 0, n \neq 0$ are termed roll modes. Such modes can be associated with the streaks that are observed in wall-bounded turbulence [25]–[30]. As characterized in physical flows these modes are seen to be counterrotating pairs of *rolls* across the span of the channel. In actual experiment they are roughly $100l_*$ in wavelength [31].

Another feature of these, as seen in Figure 2, is the very large component of velocity in the streamline direction. Thus as pointed out in [5] the counterrotating rolls are also counterflowing streamwise jets. In considering fluctuations from the mean, one finds that roll modes contain the dominant amount of energy. The roll-like structures near the walls are clearly visible on the y - z plane in Figure 2. The velocity field on the x - z plane shown at the top is located at $y = \pm 0.68$ (near the center of the rolls). It is also evident that roll-like structures correspond to alternating high- and low-speed streaks.

The remaining classification of modes, namely, $m \neq 0$, have been termed propagating modes [32], [33]. In the studies reported on in the cited references it was shown that such modes show a secular trend in phase and the result is therefore a propagation of all such modes, as it turns out at a near fixed velocity. As discussed in [5] this velocity should be the mean velocity at the location of maximal Reynolds' stress.

5. Model Dynamical Systems

Any CFD simulation is really a “reduction” of the NS equations to a dynamical system. In a modern computation one is not surprised to find such dynamical systems which substantially exceed 10^6 dynamical

equations. In this section we discuss modeling the flow by relatively few equations based on the use of empirical eigenfunctions and a Galerkin procedure.

The first such effort [6] applied this approach to the Ginzburg–Landau (GL) equation, a model fluids partial differential equation. This effort was an overwhelming success but this was fortuitous due to the fact that the GL chaotic flows which were studied were virtually free of spatial chaos. The application of the general approach to the NS equations is presented in [8]. There then follows a number of investigations in which this general approach was applied [11], [7], [20], [12]–[19]. See especially [9]. We note that while the KL mode expansion is optimum in the energy norm representation of the velocity, this does not in principle ensure that it is optimum for capturing NS dynamics. Some investigations have used KL basis functions to represent the acceleration and vorticity [34], [35]. A general discussion of the KL method is given in [36].

5.1. Galerkin Procedure

A critique of many of these approaches appears in [5], and is not repeated here. The basic procedure for determining a reduced dynamical system rests first in approximating $\tilde{\mathbf{u}}$ by a reduced set of modes, say $\{\mathbf{V}^{\mathbf{m}}(\mathbf{x})\}$, $\mathbf{m} \in S$ i.e.,

$$\tilde{\mathbf{u}} \approx \tilde{\mathbf{u}}_s = \sum_{\mathbf{m} \in S} a_{\mathbf{m}}(t) \mathbf{V}^{\mathbf{m}}(\mathbf{x}). \quad (30)$$

The Galerkin procedure is then applied,

$$(\mathbf{V}^{\mathbf{m}'}, \text{NS}(\tilde{\mathbf{u}}_s))_{\mathbf{x}} = 0, \quad (31)$$

where $\text{NS}(\tilde{\mathbf{u}}_s) = 0$ refers to the NS equations (5). The result is a system which we can write as

$$\frac{d}{dt} a_{\mathbf{m}'} = F_{\mathbf{m}'}(a_{\mathbf{m}}), \quad \mathbf{m}, \mathbf{m}' \in S. \quad (32)$$

The direction field $F_{\mathbf{m}'}(a_{\mathbf{m}})$ is at most quadratic in the dependent variables, $a_{\mathbf{m}}$. Its explicit form is given in the Appendix.

In almost all instances low-dimensional model approximations take the mean flow to be given by (15), with the Reynolds stress determined by the dynamical system. Thus $F_{\mathbf{m}'}$ is cubic in this approximation. (An exception is a study of Rayleigh–Benard convection [18]). Since our formulation is based on (5) and (30) we avoid the inconsistency (see Sections 2.3 and 6) entailed by this approximation.

5.2. Flux Velocity

We observe that there are two means for determining $\mathbf{U}(y, t)$. From the approximation (30), we get

$$\mathbf{U} \approx U_s(y, t) = \sum_{\mathbf{m}(m=n=0)} a_{\mathbf{m}}(t) \mathbf{V}^{\mathbf{m}}(\mathbf{x}). \quad (33)$$

On the other hand the Galerkin form of (14) gives another approximation of $\mathbf{U}(y, t)$. Mean flow obtained by time averaging (33) may be compared with the mean flow given by (13). It turns out that for the two determinations to be consistent, a rich enough basis is necessary. In all model systems described below, a sufficient number of flux modes is included to ensure that the two methods give nearly identical results.

5.3. Eddy Viscosity

In truncating the full NS system one limits the means for dissipating energy. As a result such a system can be expected to behave more energetically than the physical system. One remedy is the introduction of an eddy viscosity in order to facilitate energy loss by dissipation. A full discussion of this, in the present context, is given in [9].

Here we adopt a simpler, but similar approach based on energy considerations. The inner product of (5) with $\tilde{\mathbf{u}}$ integrated over the channel volume V yields

$$\frac{d}{dt} \int_V \frac{|\tilde{\mathbf{u}}|^2}{2} \frac{d\mathbf{x}}{V} = U_b(t) - \frac{1}{R_*} \int_V (|\nabla \mathbf{U}|^2 + |\nabla \mathbf{u}|^2) \frac{d\mathbf{x}}{V}. \quad (34)$$

If this is averaged in time we obtain

$$\bar{U}_b = \frac{1}{R_*} \int_V (|\nabla \bar{\mathbf{U}}|^2 + |\nabla \bar{\mathbf{u}}|^2) \frac{d\mathbf{x}}{V}, \quad (35)$$

which in dimensionless terms states that the total dissipation is equal to the mean bulk velocity. If the modes are truncated, as they will be in low-dimensional models, the energy dissipated will be altered. In order to restore this to the correct value and hence to obtain the proper value of \bar{U}_b we introduce an eddy viscosity. If we are to preserve the dimensionless form of (2), namely,

$$\frac{1}{R_*} \frac{d\bar{U}(y=-1)}{dy} = 1, \quad (36)$$

then no eddy viscosity should be introduced in (10) which also has (36) as a consequence. Instead we only introduce eddy viscosity into the fluctuation equation (11). In particular we take

$$\frac{1}{R_*} \nabla^2 \mathbf{u} \rightarrow \frac{1+e}{R_*} \nabla^2 \mathbf{u}. \quad (37)$$

where the parameter $e \geq 0$ is fixed at a value where the temporal mean of the total viscous dissipation in the model is the same as in the full simulation. In all cases, it is found that $e = 0$ gives a value of mean dissipation much lower than in the full system, indicating that the fluctuating field is too active. In addition, given a fixed value of the total dissipation, a larger system always requires smaller e as expected.

5.4. Galerkin Modes

While the Galerkin procedure is mathematically attractive its ability to produce scientific results depends in large part on the choice of functions that are included in the set S . It has been shown within this framework that false ‘‘physics’’ can appear and true physics be lost with an improper choice of modes [5], [19]. We have tried to avoid such errors.

Numerical experiments were carried out with model systems containing the following set of modes. Flux: $(m, n) = (0, 0)$, $q = 1, \dots, 32$. Fluctuations: $(m, n) = (km', ln')$, $q = 1, \dots, Q$. In all the systems $m' = 0, \pm 1, \pm 2$ and $n' = 0, \pm 1, \pm 2, \pm 3$. By letting k and l take positive integer values it is possible to construct a computational region in any desired fraction of the x - z plane of the basic wide channel ($L_x = 4\pi H$, $L_z = 4\pi H/3$). In our simulations we have chosen to take $k = l = 3$. This corresponds to a channel width of $256l_*$ containing approximately two pairs of rolls in the full simulation. Having thus determined the set of modes (m, n) to be used, models of various sizes are constructed by including an increasing number of quantum numbers for each mode. The mean velocity profiles for $Q = 2, 4, 8$, and 16 are shown in Figure 3. The number of real ODEs in these dynamical systems is (a) 92, (b) 168, (c) 304, and (d) 576. It is of interest to note that, given a system of fixed size, containing more vertical quantum numbers is more important for a low-dimensional system than having a wide range of modes with different mode numbers (m, n) .

We choose the system in Figure 3(b) as an example to illustrate further properties typical of all the systems studied. Figure 4(a) shows that the quantity $\partial U(y = -1, t)/\partial y$ computed from a low-dimensional model has the mean value R_* (with 0.41% deviation) and therefore satisfies this conservation property implied by (36). Figure 4(b) shows, for the same system, the instantaneous rates of energy added and viscous dissipation. These correspond to the first and second terms on the right-hand side of (12). In this case their averages differ by 1.58% and the difference tends to decrease with increasing time of integration. The flux and fluctuating contributions to the dissipation are also indicated in Figure 4(b). The model clearly satisfies energy conservation predicted by (17). These hold for all systems depicted in Figure 3. However, in order to maintain this level of accuracy, the model must have a minimum size comparable with the one shown in Figure 3(a).

The cross-channel distribution of Reynolds stress shown in Figure 5 is remarkable for its agreement with the full simulation. The decomposition into propagating and roll components of Reynolds stress also closely

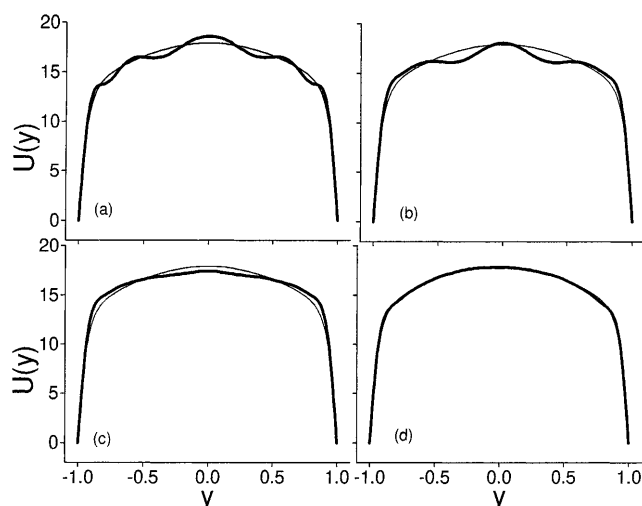


Figure 3. Comparison of the mean velocity obtained from various related dynamical systems. All the systems shown contain the same set of modes (m, n) (see (26)). The quantum numbers included for each fluctuating mode is different in each case. (a) $q \leq 2, e = 2.4$, (b) $q \leq 4, e = 1.83$, (c) $q \leq 8, e = 1.35$, (d) $q \leq 16, e = 0.853$. The mean flow obtained by (13) and by the time average of (33) are indistinguishable; both are indicated by the thicker curves in (a)–(d).

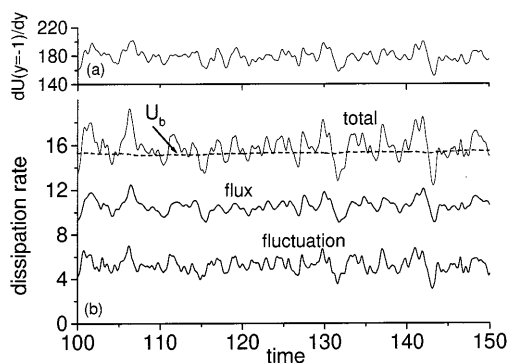


Figure 4. Momentum and energy conservation in a typical model are illustrated by (a) the skin friction, $\partial U(y = -1, t)/\partial y$; (b) the rate of energy added, $U_b(t)$, and viscous dissipation (34) calculated from the dynamical equations. This and all subsequent cases correspond to the model containing the set of modes described in Figure 3(b).

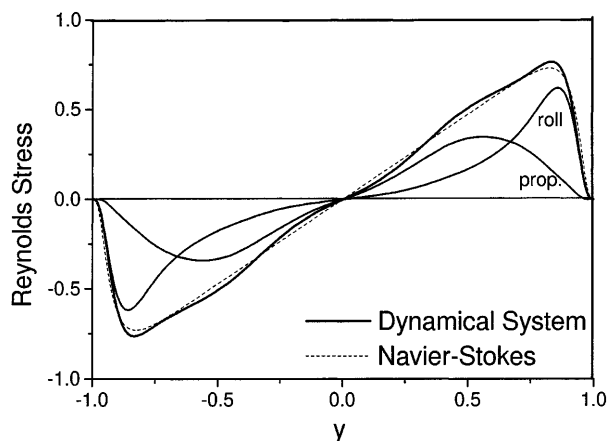


Figure 5. $\langle uv \rangle$ from the dynamical equations compared with the same quantity from the direct numerical simulation. The decomposition of the Reynolds stress into the roll- and propagating-mode components is also shown. The roll contribution which peaks near the wall indicates that roll modes (Section 4) play a greater role in viscous dissipation. The results are from the system described in Figure 3(b).

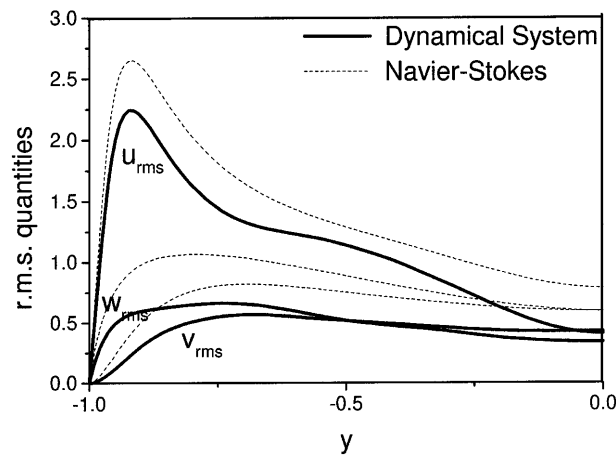


Figure 6. The half-channel distribution of r.m.s. velocities in the three coordinate directions obtained from the dynamical equations are shown. The corresponding quantities from the full simulation are shown as dashed curves. The results are from the system described in Figure 3(b).

matches the decomposition in the full simulation. The roll contribution peaks very close to the wall and plays a greater role in the transfer of energy to the fluctuating velocity components. The r.m.s. quantities plotted in Figure 6 for the half channel demonstrate the effect of truncation of modes in the dynamical system. The modes that are retained are a small fraction of those in the full system. Hence the total kinetic energy in the model must be less as seen in the figure. On the other hand, the fluctuating modes retained in the model must represent the entire fluctuating field and dissipate an equal amount of energy. Consequently, their average total kinetic energy within the model turns out to be significantly larger than the fraction captured by direct projection onto the corresponding KL modes in the full simulation. Figure 6 shows that the position of the peaks and the shape of the profile of the r.m.s. quantities in the model closely reproduce the full simulation results.

Figures 7 and 8 illustrate the phase and moduli of the modal coefficients of some of the propagating modes in the dynamical system. Propagating waves have been studied in turbulent channel flow simulations as well as in low-dimensional models [33], [13]. In the dynamical systems studied in this paper propagating waves first appear when the solution becomes periodic as R_* is increased beyond $R_* \simeq 60$. At smaller R_*

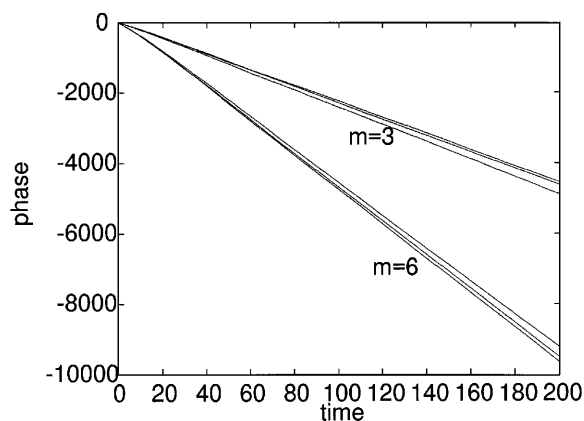


Figure 7. The phase (radians) of propagating modes has secular time-evolution. The phases of modes with $m = 3$ and $m = 6$ are shown. For each case modes with spanwise mode numbers $n = 0, 3, 6$ and $q = 1$ are shown. Each mode has a slightly different phase speed. The results are from the system described in Figure 3(b).

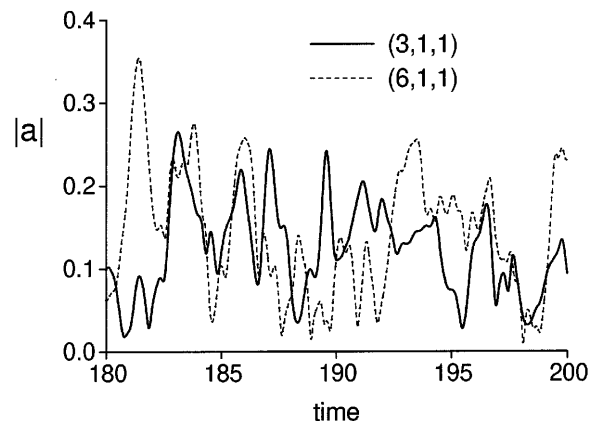


Figure 8. An example of the chaotic behavior of propagating modes. The moduli of the coefficients a_{31}^1 and a_{61}^1 from the system in Figure 7 are shown. Their phases evolve secularly as shown in Figure 7.

the system remains steady and the corresponding velocity profile is parabolic. With further increase in R_* , as the system becomes chaotic (presumably via the Ruelle–Takens scenario), the propagating waves persist on the average. The secular evolution of their phases in the turbulent regime, $R_* \simeq 180$, is illustrated by Figure 7.

For a preliminary understanding of their behavior we tentatively use the decomposition of the total velocity $\tilde{\mathbf{u}}(\mathbf{x}, t) = \bar{U}_b \mathbf{e}_x + \mathbf{u}(\mathbf{x}, t)$ and substitute this into (5). The resulting equation can be written

$$\frac{\partial \mathbf{u}}{\partial t} = -\bar{U}_b \frac{\partial \mathbf{u}}{\partial x} - \mathbf{u} \cdot \nabla \mathbf{u} - \nabla p + \frac{1}{R_*} \nabla^2 \mathbf{u} + \mathbf{e}_x. \quad (38)$$

The first term on the right is nonzero only for propagating modes since no other mode has streamwise variation. This gives an indication of the special interaction between the flux and propagating modes. We also know that \bar{U}_b tends to increase with R_* and, as a result, this interaction may dominate the right-hand side of (38) with sufficiently high R_* . In any case if we approximate (38) as $\partial \mathbf{u} / \partial t \approx -\bar{U}_b \partial \mathbf{u} / \partial x$, and substitute into this an arbitrary periodic function, $\mathbf{u} \propto e^{i(\mathbf{k} \cdot \mathbf{x} + \omega t)} + c.c.$, then \mathbf{u} turns out to be a wave propagating with streamwise velocity $c_x = -\omega / k_x \approx \bar{U}_b$. The phase speed $\omega \approx -(2\pi m / L_x) \bar{U}_b$ agrees very well with slopes of the lines in Figure 7. The roll modes ($m = 0$) appear as a degenerate case with no propagation. This is also verified by their behavior in dynamical systems. As discussed in [5] a more careful analysis of the behavior of propagating modes indicates that the wave speed should be the mean velocity at the location of maximum Reynolds stress. Interestingly this secular trend in phase coexists with chaotic behavior. The moduli of two representative propagating modes' coefficients are shown in Figure 8.

6. Further Observations and Conclusion

Figure 9 compares the behavior of the instantaneous bulk flow (18) for three different systems. The thick solid curve is calculated using the expansion (33) in the dynamical system described in Figure 3(b). The dashed curve is the result of the full simulation described in [37] performed at $R_* = 125$; hence the lower mean value of the bulk velocity. The time scales as well as the mean fluctuations of U_b in both cases appear to be very similar. These plots contrast sharply with the value of U_b from the cubic dynamical system. The latter is similar to the system in Figure 3(b) but contains no flux modes. It consists of model equations formulated by eliminating $U(y, t)$ from (11) via (15). The value of U_b in this system given by (15) turns out to be strongly time dependent (thin solid curve).

The models of channel turbulence studied in this paper have been shown to satisfy momentum and energy conservation as well as yielding the same amount of viscous dissipation found in the exact system. In addition, the mean flow and Reynolds stress profiles of the exact system is reproduced by systems containing a small fraction of the modes in the full simulation. As in the full simulation, the dynamics of the models includes modes which characterize the flux, rolls, and propagating waves. Their behavior and significance have been discussed. Unlike previous treatments the instantaneous streamwise flux is not slaved to the fluctuating flow field. It is represented by KL flux modes.

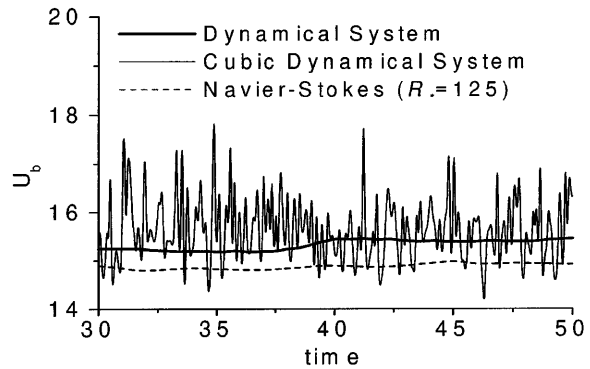


Figure 9. The instantaneous bulk velocity from three different systems. U_b based on the representation by KL flux modes in a typical dynamical system (Figure 3(b)) is shown as the thick curve. The thin curve shows the same quantity obtained from a similar system but with the mean flow eliminated from the dynamics by substituting (15) into (11). This is a cubic set of equations for the fluctuating velocity field. The dashed curve shows U_b from a direct numerical simulation [34] with $R_* = 125$.

Theoretical estimates of the dimension of the attractor for channel turbulence appear to preclude truly low-dimensional descriptions [5]. This is supported in the present results. It is found that a rich basis is necessary in order to arrive at a *consistent* representation of the mean streamwise flux and in order to satisfy momentum and energy conservation in the model equations. In particular, $O(100)$ real ordinary differential equations appear to be needed in our case to arrive at faithful descriptions of the spatial distribution of the mean flow, the Reynolds stress, and other statistical measures. When the size of the system increases, the superior convergence rate of the KL representation relative to other spectral representations begins to diminish. For example, at roughly 200 modes the Chebycheff spectral representation captures about 55% of the energy compared with 80% for the KL modes. Some of the appeal associated with applying tools of dynamical systems theory is no longer there. However, the computational advantages are still considerable. It needs to be mentioned that low-dimensional dynamics at more severe truncations do not have the conservation properties or the level of accuracy demonstrated in this paper. However, properties of the KL basis ensures that they continue to capture qualitatively features found in full simulations.

Appendix

The explicit form of the dynamical system (32) can be written

$$\frac{d}{dt}a_{kl}^q = \sum_r \mu_{kl}^{qr} a_{kl}^r + \sum_{mnrs} \beta_{klmn}^{qrs} a_{mn}^r a_{k-m,l-n}^s + g^q \delta_{k0} \delta_{l0}. \quad (\text{A1})$$

The coefficients are given in terms of KL eigenfunctions:

$$\mu_{kl}^{qr} = -\frac{1+e}{R_*} \left\{ \left[\left(\frac{2\pi k}{L_x} \right)^2 + \left(\frac{2\pi l}{L_z} \right)^2 \right] \delta_{qr} + \int_{-1}^1 \frac{d\psi_{kl}^{*q}}{dy} \cdot \frac{d\psi_{kl}^r}{dy} dy \right\}, \quad (\text{A2})$$

$$\beta_{klmn}^{qrs} = -\int_{-1}^1 \left\{ (2\pi i) (\psi_{kl}^{*q} \cdot \psi_{k-m,l-n}^s) Q_{klmn}^r + \left(\psi_{kl}^{*q} \cdot \frac{d\psi_{k-m,l-n}^s}{dy} \right) (\psi_2)_{mn}^r \right\} dy, \quad (\text{A3})$$

$$Q_{klmn}^r = \frac{k-m}{L_x} (\psi_1)_{mn}^r + \frac{l-n}{L_x} (\psi_3)_{mn}^r, \quad (\text{A4})$$

$$g^q = \int_{-1}^1 (\psi_1)_{00}^q dy. \quad (\text{A5})$$

References

- [1] Knight, B., and Sirovich, L. (1990). Kolmogorov inertial range for inhomogeneous turbulent flows. *Physics Review Letters*, **65**, 1356.
- [2] Moser, R. (1994). Kolmogorov inertial range spectra for inhomogeneous turbulence. *Physics of Fluids*, **6**, 794.
- [3] Landau, L.D., and Lifschitz, E.M. (1987). *Fluid Mechanics*. Pergamon Press Oxford.
- [4] Keefe, L., Moin, P., and Kim, J. (1992). The dimension of attractors underlying periodic turbulent Poiseuille flow. *Journal of Fluid Mechanics*, **242**, 2.
- [5] Sirovich, L. (1997). Dynamics of coherent structures in wall bounded turbulence. In *Self-Sustaining Mechanisms of Wall Turbulence*, ed. R.L. Panton. pp. 333–364. Computational Mechanics Publications, Southampton.
- [6] Sirovich, L., and Rodriguez, J.D. (1987). Coherence structures and chaos: a model problem. *Physics Letters A*, **120**(5), 211.
- [7] Aubry, N., Holmes, P., Lumley, J.L., and Stone, E. (1988). The dynamics of coherent structures in the wall region of a turbulent boundary layer. *Journal of Fluid Mechanics*, **192**, 115.
- [8] Sirovich, L. (1987). Turbulence and the dynamics of coherent structures, Parts i–iii. *Quarterly of Applied Mathematics*, **45**, 561.
- [9] Holmes, P., Lumley, J.L., and Berkooz, G. (1996). *Turbulence, Coherent Structures, Dynamical Systems and Symmetry*. Cambridge University Press, Cambridge.
- [10] Berkooz, G., Holmes, P., and Lumley, J.L. (1993). The proper orthogonal decomposition in the analysis of turbulent flows. *Annual Review of Fluid Mechanics*, **25**, 539.
- [11] Chambers, D.H., Adrian, R.J., Moin, P., Stewart, D.S., and Sung, H.J. (1988). Karhunen–Loeve expansion of burgers model of turbulence. *Physics of Fluids*, **31**, 2573.

- [12] Holmes, P. (1990). Can dynamical systems approach turbulence. In *Whither Turbulence? Turbulence at the Crossroads*, ed. J.L. Lumley, page 195. Springer-Verlag, New York.
- [13] Zhou, X., and Sirovich, L. (1992). Coherence and chaos in a model of turbulent boundary layer. *Physics of Fluids A*, **4**, 2855.
- [14] Rajaei, M., Karlsson, S.K.F., and Sirovich, L. (1994). Low-dimensional description of free-shear-flow coherent structures and their dynamical behaviour. *Journal of Fluid Mechanics*, **258**, 1.
- [15] Rempfer, D., and Fasel, H.F. (1994). Dynamics of three-dimensional coherent structures in a flat plate boundary layer. *Journal of Fluid Mechanics*, **275**, 257.
- [16] Liakopoulos, A., and Gunes, H. Low-order dynamical models of thermal convection in high-aspect ratio enclosures. *Journal of Fluid Mechanics*, to appear.
- [17] Tarman, I.H., and Sirovich, L. (1998) Extensions to Karhunen–Loeve based approximations of complicated phenomena. *Computer Methods in Applied Mechanics and Engineering*, **155**(3–4), 359–368.
- [18] Tarman, I.H., and Sirovich, L. A parametric study of Rayleigh–Benard convection using a Karhunen–Loeve basis. Submitted for publication.
- [19] Sirovich, L., and Zhou, X. (1994) Dynamical model of wall-bounded turbulence. *Physical Review Letters*, **72**, 340.
- [20] Deane, A.E., Kevrekidis, I.G., Karniadakis, G.E., and Orszag, S.A. (1991). Low-dimensional models for complex geometry flows: application to grooved channels and circular cylinders. *Physics of Fluids*, **3**(10), 2337.
- [21] Ball, K.S. Sirovich, L., and Keefe, L.R. (1991). Dynamical eigenfunction decomposition of turbulent channel flow. *International Journal for Numerical Methods in Fluids*, **12**, 585.
- [22] Sirovich, L., and Zhou, X. (1994). Reply to “Observations regarding ‘Coherence and chaos in a model of turbulent boundary layer’ by X. Zhou and L. Sirovich.” *Physics of Fluids A*, **6**, 1579.
- [23] Jimenez, J., and Moin, P. (1991). The minimal flow unit in near-wall turbulence. *Journal of Fluid Mechanics*, **225**, 213.
- [24] Kim, J., Moin, P., and Moser, R. (1987). Turbulence statistics in fully developed channel flow at low Reynolds number. *Journal of Fluid Mechanics*, **177**, 133.
- [25] Kline, S.J., Reynolds, W.C., Schraub, F.A., and Runstadler, P.W. (1967). The structure of turbulent boundary layers. *Journal of Fluid Mechanics*, **95**, 741.
- [26] Kim, H.T., Kline, S.J., and Reynolds, W.C. (1971). The production of turbulence near a smooth wall in a turbulent boundary layer. *Journal of Fluid Mechanics*, **50**, 133.
- [27] Smith, C.R., and Metzler, S.P. The characteristics of low-speed streaks in the near-wall region of a turbulent boundary layer. *Journal of Fluid Mechanics*, **129**, 27.
- [28] Smith, C.R., and Schwartz, S.P. (1983). Observation of streamwise rotation in the near-wall region of a turbulent boundary layer. *Physics of Fluids*, **26**(3), 641.
- [29] Robinson, S.K. (1991). Coherent motions in the turbulent boundary layer. *Annual Review of Fluid Mechanics*, **23**, 601.
- [30] Cantwell, B.J. Organized motion in turbulent flow. *Annual Review of Fluid Mechanics*, **13**, 437.
- [31] Blackwelder, R.F., and Kaplan, R.E. (1976). On the wall structure of the turbulent boundary layer. *Journal of Fluid Mechanics*, **76**, 89.
- [32] Sirovich, L., Ball, K.S., and Handler, R.A. (1991) Propagating structures in wall-bounded turbulent flows. *Theoretical and Computational Fluid Dynamics*, **2**, 307.
- [33] Sirovich, L., Ball, K.S. and Keefe, L.R. (1990). Plane waves and structures in turbulent channel flow. *Physics of Fluids*, **2**(12), 2217.
- [34] Sirovich, L., Knight, B.W., and Rodriguez, J.D. (1990). Optimal low dimensional dynamical approximations. *Quarterly of Applied Mathematics*, **48**(3), 535.
- [35] Sirovich, L. Empirical eigenfunctions and low dimensional systems. In *New Perspectives in Turbulence*, ed. L. Sirovich, page 139. Springer-Verlag, New York, 1991.
- [36] Kirby, M. (1992). Minimal dynamical systems from PDEs using Sobolev eigenfunctions. *Physica D*, **57**, 466.
- [37] Handler, R.A., Levich, E., and Sirovich, L. (1993). Drag reduction in turbulent channel flow by phase randomization. *Physics of Fluids*, **5**(3), 686.